

ARTICLE


<https://doi.org/10.1038/s41467-021-23310-w>

OPEN

Superconductivity emerging from a stripe charge order in IrTe_2 nanoflakes

Sungyu Park^{1,14}, So Young Kim^{1,2,14}, Hyoung Kug Kim², Min Jeong Kim^{1,3}, Taeho Kim^{1,3}, Hoon Kim^{1,2}, Gyu Seung Choi^{1,2}, C. J. Won^{4,5}, Sooran Kim⁶, Kyoo Kim⁷, Evgeny F. Talantsev^{8,9}, Kenji Watanabe¹⁰, Takashi Taniguchi¹¹, Sang-Wook Cheong^{4,5,12}, B. J. Kim^{1,2}, H. W. Yeom^{1,2}, Jonghwan Kim^{1,2,3✉}, Tae-Hwan Kim^{2,5,13✉} & Jun Sung Kim^{1,2✉}

Superconductivity in the vicinity of a competing electronic order often manifests itself with a superconducting dome, centered at a presumed quantum critical point in the phase diagram. This common feature, found in many unconventional superconductors, has supported a prevalent scenario in which fluctuations or partial melting of a parent order are essential for inducing or enhancing superconductivity. Here we present a contrary example, found in IrTe_2 nanoflakes of which the superconducting dome is identified well inside the parent stripe charge ordering phase in the thickness-dependent phase diagram. The coexisting stripe charge order in IrTe_2 nanoflakes significantly increases the out-of-plane coherence length and the coupling strength of superconductivity, in contrast to the doped bulk IrTe_2 . These findings clarify that the inherent instabilities of the parent stripe phase are sufficient to induce superconductivity in IrTe_2 without its complete or partial melting. Our study highlights the thickness control as an effective means to unveil intrinsic phase diagrams of correlated van der Waals materials.

¹Center for Artificial Low Dimensional Electronic Systems, Institute for Basic Science, Pohang, Korea. ²Department of Physics, Pohang University of Science and Technology, Pohang, Korea. ³Department of Materials Science and Engineering, Pohang University of Science and Technology, Pohang, Korea. ⁴Laboratory for Pohang Emergent Materials, Pohang Accelerator Laboratory, Pohang, Korea. ⁵Max Planck POSTECH/Korea Research Initiative, Pohang, Korea. ⁶Department of Physics Education, Kyungpook National University, Daegu, Korea. ⁷Korea Atomic Energy Research Institute (KAERI), Yuseong-gu, Daejeon, Korea. ⁸M.N. Mikheev Institute of Metal Physics, Ural Branch, Russian Academy of Sciences, Ekaterinburg, Russia. ⁹NANOTECH Centre, Ural Federal University, Ekaterinburg, Russia. ¹⁰Research Center for Functional Materials, National Institute for Materials Science, Tsukuba, Japan. ¹¹International Center for Materials Nanoarchitectonics, National Institute for Materials Science, Tsukuba, Japan. ¹²Rutgers Center for Emergent Materials and Department of Physics and Astronomy, Rutgers University, Piscataway, NJ, USA. ¹³Asia Pacific Center for Theoretical Physics (APCTP), Pohang, Korea. ¹⁴These authors contributed equally: Sungyu Park, So Young Kim. ✉email: jonghwankim@postech.ac.kr; taehwan@postech.ac.kr; js.kim@postech.ac.kr

Transition metal dichalcogenides (TMDCs) provide a prototypical quasi-two-dimensional system, possessing various electronic instabilities to periodic charge modulations¹. These instabilities often induce complex charge-density-wave (CDW) phases with different commensurability conditions^{2–5}, sometimes associated with Mott² or excitonic insulating⁶ phases. Upon chemical doping^{4,5,7,8}, these phases are commonly driven into a superconducting phase, resulting in a characteristic dome-shaped phase diagram, reminiscent of those found in other unconventional superconductors^{9–11} (Fig. 1a). Understanding the complex interplay between charge ordering and superconducting instabilities in TMDCs is a long standing issue, which has often been hampered by presence of quenched disorders, introduced in chemical doping. Recently, utilising the weak van der Waals (vdW) coupling between layers, TMDCs were found to be thinned down to atomic length scale¹², comparable with the coherence lengths of their various electronic orders. This offers another effective way to tune stability or properties of the competing phases, as demonstrated for 1T-TaS₂^{13–15} and NbSe₂^{16,17}, in which distinct thickness dependence of the transition temperatures is observed for superconducting and CDW phases.

IrTe₂ is one of the TMDCs in vdW structure (Fig. 1b), showing a similar dome-shaped superconducting phase diagram^{18–23}. IrTe₂ undergoes a stripe charge ordering transition at $T_s \sim 260$ K, and by suppressing it with e.g. chemical doping^{18–23} the superconducting phase eventually appears, similar to TMDCs hosting the parent CDW orders^{4,5,7,8}. The stripe order in IrTe₂, however, is accompanied by the first-order structural transition involving in-plane Ir–Ir dimerization and interlayer Te–Te depolymerisation^{24,25}, which forms stripe patterns with a predominant period of $5a_0$ (a_0 , the a axis lattice constant) as depicted in Fig. 1c and d^{19,26}. No clear evidence of gap opening in the Fermi surface (FS) is observed^{27,28}, unlike the typical CDW gap

formation in TMDCs²⁹. Instead, FS reconstruction to the so-called cross-layer two-dimensional (2D) state^{30,31} occurs due to suppression of the density of states (DOS) in the planes of Ir–Ir dimers running across the vdW gaps. These aspects suggest that the relationship between the stripe and superconducting orders in IrTe₂ may differ significantly from those of other TMDCs, as indicated by recent discoveries on the superconductivity in quenched or thinned IrTe₂ crystals^{32–34}. Here using Raman spectroscopy, scanning tunnelling microscopy, and transport property measurements, we found that the parent stripe phase encompasses the whole superconducting dome in the thickness-dependent phase diagram (Fig. 1a). This unusual coexistence of the stripe and superconducting orders significantly increases the interlayer coherence length and the coupling strength of superconductivity in IrTe₂ nanoflakes, revealing the collaborative role of the stripe order to the superconductivity in IrTe₂.

Results

Thickness dependent phase transitions. In order to vary the thickness of IrTe₂, we employed the mechanical exfoliation method of single crystals and obtained thin flakes with thickness (d) down to ~ 10 nm, which show a systematic thickness dependence of the in-plane resistivity ρ (Fig. 1e). For the temperature sweeps in both directions, we took a slow cooling rate of ~ 0.5 K/min, in order to minimise inhomogeneous domain formation of the stripe-charge-ordered and charge-disordered phases, found in rapid-cooled IrTe₂ crystals^{32,33,35}. The temperature dependent $\rho(T)$ follows a metallic temperature dependence with abrupt changes at $T_{s,dn}$ and $T_{s,up}$, due to the first-order stripe ordering transition as found in bulk crystals^{24,25}. These resistive anomalies across the transitions, however, become much smaller in size with reducing d , and eventually disappears for $d < 50$ nm. This does not mean full suppression of

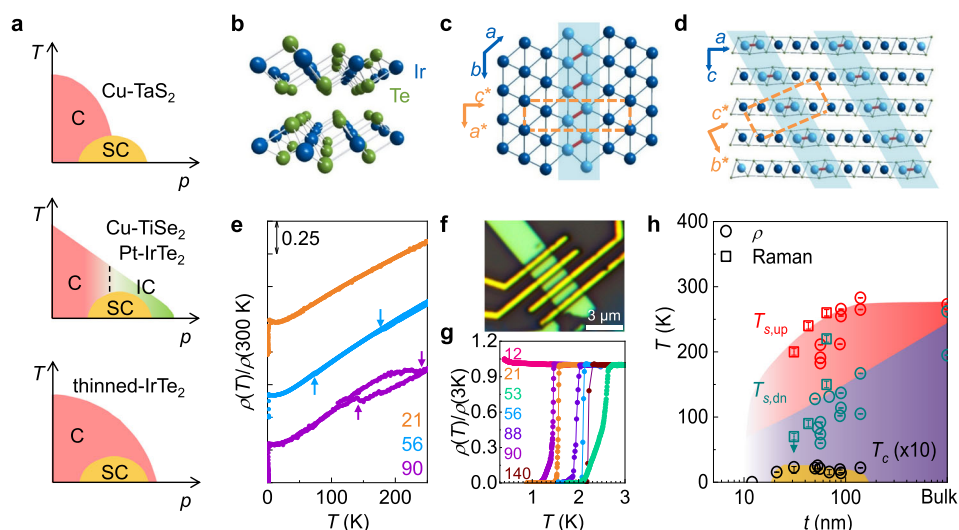


Fig. 1 Structure and phase diagram of IrTe₂ nanoflakes. **a** Schematic phase diagrams of TMDCs as a function of control parameter p , showing commensurate (C), incommensurate charge order (IC), and superconductivity (SC). Three different types of dome-shaped superconducting phase diagram, where the dome lies at the centre of a presumed quantum critical point (top), near the C-IC transition line (middle), or well inside the parent order (bottom). **b** Crystal structure of IrTe₂. **c, d** Schematic illustrations of the stripe order in IrTe₂ below T_s . The Ir–Ir dimerization (red) with a modulation vector $\mathbf{q} = (\frac{1}{5}, 0, \frac{1}{2})$ is depicted (blue shade) on the triangular Ir layer (**c**) and across the stacked layers (**d**). The crystallographic axes for the high- T (**a, b**, and **c**) and the low- T (a^* , b^* , and c^*) structures are shown, together with the unit cell of the stripe phase (orange box). **e** Temperature dependence of the normalised resistivity $\rho(T)/\rho(300\text{ K})$ for IrTe₂ crystals with thickness (d) of 21, 56, and 90 nm. For clarity, $\rho(T)/\rho(300\text{ K})$ curves are offset vertically. Transition temperatures $T_{s,up}$ and $T_{s,dn}$ are determined (arrows) in opposite temperature sweeps. **f** Optical microscope image of a 56-nm-thick IrTe₂ crystal. **g** $\rho(T)/\rho(3\text{ K})$ curves for IrTe₂ crystals with $d = 12\text{--}140$ nm. **h** Phase diagram of IrTe₂ nanoflakes as a function of thickness d , obtained by transport (circle) and Raman spectroscopy (square) measurements. The transition temperatures $T_{s,up}$ (red) and $T_{s,dn}$ (blue) during warming and cooling are plotted with the superconducting transition temperature T_c (black), scaled by a factor of 10 for clarity. The error bars from the resistivity and Raman spectroscopy are defined by the width of the corresponding resistive transitions and the temperature step of 5 K between the measurements, respectively.

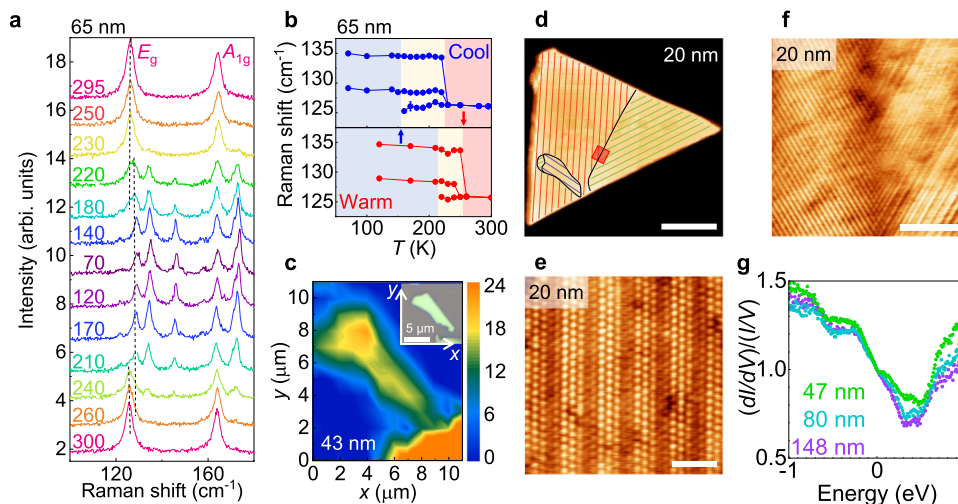


Fig. 2 Stripe charge ordering formation in IrTe₂ nanoflakes. **a**, **b** Raman spectra (**a**) and corresponding temperature dependent Raman frequency (**b**) of a 65-nm-thick IrTe₂ nanoflake at various temperatures during cool-down and warm-up procedures. At $T < T_s$, the Raman modes, E_g at 126 cm⁻¹ and A_{1g} at 165 cm⁻¹, split into multiple peaks as the flake forms the stripe charge order in **a**. The temperature ranges for the normal (red), the stripe (blue), and intermediate coexistence (yellow) phases, are identified in **b**, during cooling (upper panel) and warming (lower panel). Transition temperatures $T_{s,dn}$ and $T_{s,up}$ are indicated by the arrows, respectively. **c** Spatial profile of Raman intensity map for 129 cm⁻¹ for a 43-nm-thick IrTe₂ nanoflake at $T \sim 70$ K. Inset: optical microscope image of the flake. **d** Large-scale scanning tunnelling microscopy (STM) image of a 20-nm-thick IrTe₂ flake at $T = 85$ K (scale bar, 300 nm). The flake has only stripe-phase charge-ordered domains, illustrated by red, green, and blue lines. Black lines indicate domain boundaries between three equivalent stripe-phase charge-ordered domains. **e** Atomically resolved STM image of **d** at $T = 85$ K representing a uniform striped area with 5×1 surface reconstruction (scale bar, 2 nm). **f** Zoomed-in STM image of two charge-ordered phases indicated by red square in **d** showing that the two phases coexist at the boundary (scale bar, 20 nm). **g** Scanning tunnelling spectroscopy (STS) spectra at $T = 85$ K taken on IrTe₂ nanoflakes with $d = 47, 80$, and 148 nm, as indicated in the plot.

the stripe order in thin nanoflakes, since the size of the resistive anomaly is known to be strongly suppressed by introducing strain, reducing the sample volume, and increasing the cooling rate even in bulk samples³⁴. Rather, the stripe order is found to be stable in all the nanoflakes we studied, as discussed below (Fig. 2). At low temperatures, all the nanoflakes, except the thinnest one with $d = 12$ nm, exhibit a superconducting transition as found in the temperature-dependent normalised resistance $\rho(T)/\rho(3\text{ K})$ (Fig. 1g). The superconducting transition temperature, defined as a 50% resistive transition, is $T_c = 1.43\text{--}2.64$ K, somewhat lower than $T_c \sim 3$ K for the optimally doped bulk IrTe₂^{18,19}, mostly due to the 2D nature as discussed below (Fig. 3). Unlike the stripe charge ordering transition, the superconductivity is found to be quite stable in nanoflakes. The superconducting transition temperatures and widths remain almost the same in different thermal cycling (Supplementary Fig. 7).

The stripe ordering transition of IrTe₂ nanoflakes is characterised by Raman spectroscopy. For bulk IrTe₂, two Raman active modes, E_g at 126 cm⁻¹ and A_{1g} at 165 cm⁻¹, in a trigonal structure (space group $P\bar{3}m1$) split into multiple peaks due to the lowered symmetry and the emergence of a super unit cell for the stripe order below T_s ^{30,36}. Raman spectra taken from the 65-nm-thick nanoflake with sequential decrease and increase of temperature (Fig. 2a) reveal that both E_g and A_{1g} Raman modes at room temperature split into multiple Raman modes at $T = 70$ K, well below T_s , consistent with previous studies on the bulk³⁶. This behaviour is also shown for the flakes with different thicknesses (Supplementary Fig. 2a and Fig. 3a) and confirms formation of the stripe charge order in our IrTe₂ nanoflakes.

In IrTe₂ nanoflakes, however, the temperature dependence of the stripe phase evolution is distinct from the bulk case. We found that below T_s there is an intermediate temperature range (yellow range in Fig. 2b) where the high temperature Raman modes coexist with the low temperature modes, for both temperature sweeps. This contrasts to the abrupt change found

in bulk IrTe₂ with a negligible coexistence range³⁶ and indicates macroscopic phase separation of the normal and stripe phases in IrTe₂ nanoflakes at the intermediate temperature. We defined $T_{s,dn}$ and $T_{s,up}$ as the temperatures where the contribution from the normal and stripe phase disappears during the cool-down and warm-up procedures, respectively (Fig. 2b). As the flake thickness decreases, the transition temperatures monotonically decrease, which are in good agreement with those from $\rho(T)$ (Fig. 1h). In addition, we measured the Raman spectroscopy on IrTe₂ flakes, cooled down to $T = 4$ K, just above $T_c \sim 2$ K. For IrTe₂ flakes with various thicknesses from 10 nm to 174 nm, which cover the whole superconducting dome in the thickness-dependent phase diagram, we observed clear splitting of Raman modes, consistent with the stripe-charge-order formation (Supplementary Fig. 3). These results clearly show that the region of the stripe phase overlaps with the entire superconducting dome in a wide range of thickness.

Coexistence of stripe order and superconductivity. This phase diagram significantly differs from the doping-dependent phase diagram of bulk IrTe₂^{18–23}. In the bulk case, the stripe and superconducting phases are mutually exclusive, and the coexisting region appears in the very narrow doping range^{18–23}. Even in this coexisting phase, two ordered phases are macroscopically separated^{22,23}. Such a macroscopic phase separation is also suggested in the super-cooled case^{32,33,35}. However, in IrTe₂ nanoflakes, the stripe phase completely covers the whole regions of the sample, as confirmed by the spatial mapping of Raman signal, taken at ~ 70 K well below T_s (Fig. 2c). The intensity map of the 129 cm⁻¹ Raman mode, which is the hallmark of the stripe phase, reveals a strong Raman intensity profile over the entire nanoflake as in the optical microscope image (Fig. 2c inset), while the signal from the normal phase is absent (Supplementary Fig. 2c). This indicates that the stripe phase dominantly prevails in the

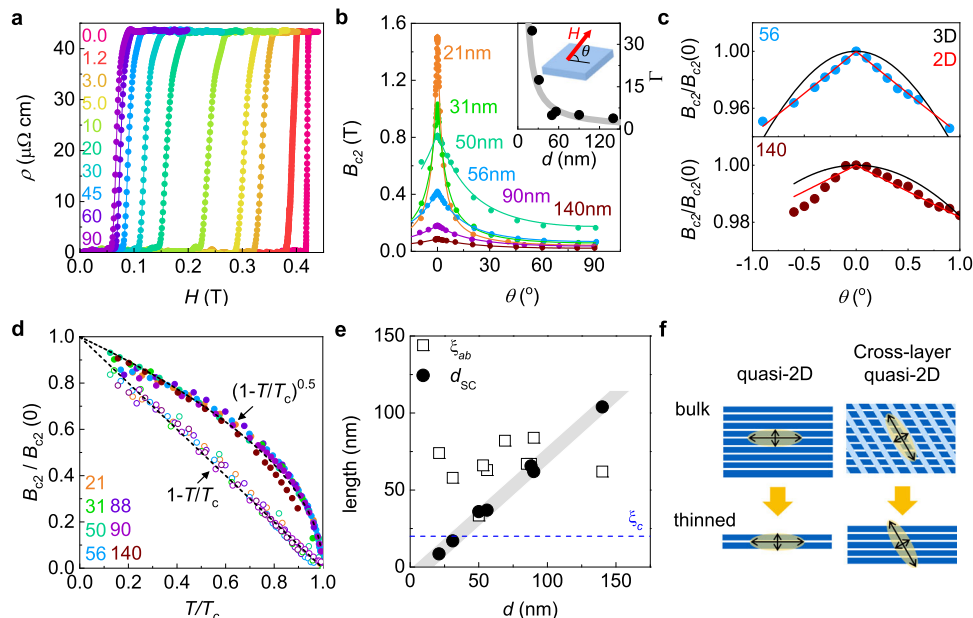


Fig. 3 Two dimensional superconductivity of IrTe₂ nanoflakes. **a**, Magnetic field dependence of $\rho(H)$ of a 56-nm-thick IrTe₂ nanoflake, measured with different field orientations θ at $T = 0.35$ K. **b**, Upper critical field B_{c2} as a function of field angle θ for IrTe₂ nanoflakes with different thickness (d) at $T = 0.35$ K, together with the fit (solid line) to the 2D Tinkham model. Inset: the anisotropy factor $\Gamma = B_{c2}^{ab}/B_{c2}^c$ as a function of d , following $1/d$ dependence (grey line). Schematic illustration shows the field orientation θ . **c**, Angle dependence of $B_{c2}(\theta)$ of IrTe₂ nanoflakes with $d = 56$ and 140 nm at $T = 0.35$ K. Good agreement with the 2D Tinkham model (red), rather than the 3D Ginzburg-Landau model (black), confirms the 2D superconductivity. **d**, Normalised $B_{c2}/B_{c2}(0)$ as a function of T/T_c for IrTe₂ nanoflakes with different d . All data collapse into dashed lines described by $1 - T/T_c$ and $(1 - T/T_c)^{1/2}$ for B_{c2}^c (open circles) and B_{c2}^{ab} (solid circles), respectively. **e**, Ginzburg-Landau coherence length ξ_{ab} (square) and the effective superconducting thickness d_{sc} (circle) as a function of d . ξ_{ab} is nearly independent of d , whereas d_{sc} grows linearly with d ($d_{sc} \sim 0.8d$) and exceeds ξ_c of doped bulk IrTe₂. **f**, Schematic illustration of the size effect of vdW superconductors with a large anisotropy $\xi_c \ll \xi_{ab}$. 2D superconductivity appears only for a few-layer-thick crystals. In IrTe₂ with a stripe order and the resulting cross-layer quasi-2D state, the increased $\xi_c \sim \xi_{ab}$ induces 2D superconductivity in relatively thick nanoflakes.

macroscopic length scale and serves as a normal state for the superconductivity, in contrast to the doped bulk IrTe₂ case.

The dominant stripe phase formation is further confirmed by scanning tunnelling microscopy (STM) for a representative nanoflake with $d = 20$ nm (Fig. 2d). At room temperature, the hexagonal lattice of top-most Te atoms is clearly resolved by STM in all IrTe₂ nanoflakes (Supplementary Fig. 4b). When cooled down below the stripe ordering temperature ($T_{STM} = 85$ K $< T_s$), the ultrathin nanoflake develops clear stripe patterns with a period of $5a_0$ due to the charge ordering and dimerization of Ir atoms (Fig. 2e), as observed in bulk crystals^{25,26}. By scanning over the nanoflake with sufficient spatial resolution (Fig. 2f), we confirm that the whole surface of the flake hosts one or two predominant stripe phases among three energetically equivalent phases (Fig. 2d), and the stripe patterns are often oriented nearly parallel to the long edges of nanoflakes. In thicker nanoflakes (Supplementary Fig. 5a), stripe domain patterns became more complex, similar to bulk IrTe₂³⁵. We note that even with fast cooling at ~ 1 K/sec, neither thin nor thick nanoflakes show the hexagonal phase that is often observed in either super-cooled or doped bulk IrTe₂^{22,35} and considered to be responsible for the superconductivity. Consistently, in the scanning tunnelling spectroscopy (STS) measurements on IrTe₂ nanoflakes, we observe similar local DOS over the wide range of thicknesses. In STS spectra (Fig. 2g), obtained on different IrTe₂ nanoflakes with $47 \leq d \leq 148$ nm, the local spectral features are qualitatively consistent with the total DOS for the stripe phase of bulk IrTe₂, as estimated using first principle calculations³⁰. Our results from STM and Raman spectroscopy provide strong evidence that the

superconductivity emerges from the preexisting stripe phase in IrTe₂ nanoflakes.

2D superconductivity. Now we focus on the effect of the underlying stripe order on the superconducting properties. To address this issue, we investigated the upper critical field B_{c2} of each nanoflake as a function of field orientation below T_c . Figure 3a shows the resistivity $\rho(H)$ curves of a representative nanoflake with $d = 56$ nm, collected at $T = 0.35$ K under a magnetic field, for which the angle θ is defined with respect to the ab plane. The anisotropy of B_{c2} , $\Gamma = B_{c2}^{ab}/B_{c2}^c \sim 5.3$ for $d = 56$ nm, becomes stronger with lowering d and reaches up to $\Gamma \sim 38$ for $d = 21$ nm (Fig. 3b), an order of magnitude larger than $\Gamma \sim 2$ of doped bulk IrTe₂³⁷. This large increase in Γ with moderate changes in T_c (Fig. 1g) and the in-plane coherence length $\xi_{ab}(0)$ (Fig. 3e) can only be explained by 2D superconductivity. In the Tinkham model of 2D superconductivity³⁸, the angle dependent $B_{c2}(\theta)$ at the zero-temperature limit is described by $|B_{c2}(\theta) \sin \theta / B_{c2}^c| + (B_{c2}(\theta) \cos \theta / B_{c2}^{ab})^2 = 1$, where $B_{c2}^{ab} = (\sqrt{12}\Phi_0)/(2\pi\xi_{ab}(0)d_{sc})$ and $B_{c2}^c = \Phi_0/(2\pi\xi_{ab}(0)^2)$ (Φ_0 , a flux quantum). Thus by reducing the effective thickness of the superconducting layer d_{sc} , Γ becomes large with a constant $\xi_{ab}(0)$, and a discontinuous cusp in the $B_{c2}(\theta)$ curve near $\theta = 0^\circ$ is expected. These predictions are distinct from those of the Ginzburg-Landau model for anisotropic three-dimensional (3D) superconductors³⁸, as described by $B_{c2}(\theta) = B_{c2}(0^\circ)/\sqrt{\Gamma^2 \sin^2 \theta + \cos^2 \theta}$. All $B_{c2}(\theta)$ curves exhibit a clear cusp near $\theta = 0^\circ$ and are successfully fitted by the 2D Tinkham model rather than the anisotropic 3D model (Fig. 3b and Supplementary

Fig. 9). For $d = 140$ nm, the thickest sample, $B_{c2}(\theta)$ slightly deviates from the 2D model, but still far from 3D model (Fig. 3c). These results demonstrate that IrTe₂ nanoflakes with $d \leq 140$ nm clearly show the 2D superconductivity.

The temperature dependence of $B_{c2}(T)$ under in-plane ($B \parallel ab$) and out-of-plane ($B \parallel c$) magnetic fields further confirms the 2D superconductivity of IrTe₂ nanoflakes. For seven samples with different d 's, we determined $B_{c2}(T)$ by taking 50% of the resistive transition as a function of the normalised temperature $t = T/T_c$ (Fig. 3d and Supplementary Fig. 8). The out-of-plane $B_{c2}^c(t)$ is almost the same, following the linear dependence (Fig. 3d), as observed in the doped bulk sample³⁷. The in-plane $B_{c2}^{ab}(t)$ increases strongly with lowering d , but the normalised $B_{c2}(t)/B_{c2}(0)$ curves for all samples collapse into a single curve following the 2D Ginzburg-Landau model³⁸, $B_{c2}^{ab}(t) = \frac{\Phi_0 \sqrt{12}}{2\pi \xi_{ab} d_{SC}} (1 - t)^{1/2}$. Using $\xi_{ab}(0)$, estimated from the observed $B_{c2}^c(0)$, we obtained d_{SC} is $\sim 80\%$ of the measured thickness d (Fig. 3e). Considering that 2D superconductivity is induced at d ($\sim d_{SC}$) smaller than the out-of-plane coherence length ξ_c , i.e. $d < \xi_c$, we conclude that $\xi_c(0)$ of IrTe₂ nanoflakes should be larger than the maximum value of $d_{SC} \sim 100$ nm, obtained in experiments (Fig. 3e). This value is significantly larger than the typical $\xi_c(0) \sim 25$ nm of doped IrTe₂ bulk samples³⁷, and comparable to the in-plane coherence length $\xi_{ab}(0) \sim 70$ nm³⁹ (Fig. 3e). These findings clearly indicate that the superconducting characteristics of IrTe₂ nanoflakes are distinct from those of the doped IrTe₂.

Characteristics of superconductivity coexisting stripe order.

The drastically increased $\xi_c(0)$ in IrTe₂ nanoflakes is a consequence of the coexisting stripe order. In anisotropic superconductors, the interlayer coherence length $\xi_c(0)$ is determined by the superconducting gap (Δ_{SC}) and the Fermi velocity (v_F^c), i.e. $\xi_c(0) \propto v_F^c / \Delta_{SC}$. Assuming a similar Δ_{SC} , $\xi_c(0)/\xi_{ab}(0) \approx v_F^c/v_F^{ab} \gtrsim 1$ seems incompatible with the vdW structure of IrTe₂. This however can be explained by considering the coexisting stripe order. In the stripe phase of IrTe₂, Ir-Ir dimerization and Te-Te depolymerisation produce conducting planes between the dimer planes, running across the vdW gaps (Fig. 1d). This cross-layer 2D conducting state³⁰ affects the electronic structure such that the interlayer v_F^c is even larger than the in-plane v_F^{ab} , which greatly increases $\xi_c(0)$ (Fig. 3f). Unlike the conventional vdW superconductors in which 2D superconductivity can only be induced in a few-layer-thick crystals, IrTe₂ hosts 2D superconductivity in the relatively thick crystals due to the microscopically coexisting stripe order.

The distinct superconducting nature in IrTe₂ nanoflakes is also found in their superconducting gap as compared to the doped bulk. Figure 4a presents the current-voltage (IV) characteristics at different temperatures for a representative nanoflake with $d = 21$ nm. Near $T_c \approx T_{BKT}$, they follow Berezinskii-Kosterlitz-Thouless transition for 2D superconductivity (Fig. 4b), in which the exponent α extracted from $V \propto I^\alpha$ crosses $\alpha = 3$ at T_{BKT} . Well below T_c , the self-field critical current density $J_{c,sf}(T)$ can be obtained from the IV characteristics with variation of temperature, which is proportional to temperature dependent London penetration depth $\lambda(T)$ for $d \ll \lambda$ ^{40,41}. From the critical current $I_c(T)$, at which the measured voltage jumps due to the superconducting-to-normal transition, we obtained the corresponding $J_{c,sf}(T)$ and $\lambda(T)$ curves (Fig. 4c and Supplementary Fig. 10), which can be nicely reproduced by the fit based on BCS theory using $\Delta_{SC} \approx 0.38$ meV. The superconducting gap (Δ_{SC}), taken from IrTe₂ nanoflakes with different thicknesses, varies linearly with their T_c with a superconducting gap ratio of $2\Delta_{SC}/k_B T_c \sim 5.3$, which is much larger than the BCS

value of 3.53 and $2\Delta_{SC}/k_B T_c \sim 3.7$ of doped bulk IrTe₂^{37,42} (Fig. 4d). Thus, superconductivity in IrTe₂ nanoflakes is in the strong coupling regime, whereas that of doped bulk IrTe₂ is in the weak coupling regime.

Discussion

Our findings unequivocally emphasise that the superconductivity in IrTe₂ nanoflakes, which emerges from the preexisting stripe order, is highly distinct from that in doped bulk IrTe₂. On pristine IrTe₂ bulk or surface, the $5a_0$ stripe phase undergoes multiple transitions to other nearly-degenerate stripe phases that have different periods such as $8a_0$ and $6a_0$, and also a honeycomb phase^{35,43–45}. The complex stripe ordering formation is a result of subtle balance between local interactions of Ir-Ir dimerization and Te-Te depolymerisation. These incipient instabilities and the resulting strong electron-lattice coupling of the parent $5a_0$ stripe phase can facilitate pairing interaction for superconductivity in a proper condition and thereby enhancing the superconducting coupling strength as observed in IrTe₂ nanoflakes. This coexisting phase of stripe and superconducting orders, however, cannot be accessed by chemical doping, e.g. Pt doping at the Ir sites. A few % of doping directly perturbs Ir dimerization and melts the stripe order to a quasi-periodic hexagonal order^{18,22}. In this case, the onset of superconductivity coincides with disorder-induced melting of the parent order²³, reminiscent of other TMDCs such as Cu-doped TiSe₂^{3–5}.

In contrast, the thickness control of IrTe₂ tunes the stripe order without introducing quenched disorders. The stripe order in IrTe₂ may be mildly suppressed by the thinning-induced out-of-plane elongation^{13,46} or the substrate-induced in-plane tensile strain as opposite to the pressure effect enhancing T_s ²⁴. Typically, the thinning-induced out-of-plane elongation of $\Delta c/c \sim 0.1\%$, as found in TaS₂^{13,46} and the substrate-induced in-plane strain of $\Delta a/a \sim 0.1–0.3\%$ (Supplementary Note 6) are expected in the thinned IrTe₂, where a and c are the in-plane and out-of-plane lattice constants, respectively. A recent study on a strained IrTe₂ single crystals⁴⁷ revealed that only $\sim 0.1\%$ of tensile strain induces the transition between the stripe-charge-ordered phases with different periods of $5a_0$ and $6a_0$, which significantly modifies the electronic structures. Our first principle calculations for electron-phonon coupling constant λ_{ep} of the $5a_0$ stripe phase show that the in-plane tensile strain is more effective to drive the system to the structural instability and to enhance λ_{ep} than the out-of-plane elongation, which increases T_c by a factor of ~ 3 (Supplementary Table 1). While the corresponding critical strain is much larger in calculations and also the calculated T_c remains lower than the measured $T_c \sim 2$ K, these observations imply that the stripe phase of IrTe₂ is intrinsically in close proximity to the superconducting phase, which can be accessed by reducing thickness or by thermal quenching^{32,33}. It has been known that, in the vicinity of full charge order melting, strong electron-phonon coupling^{48,49} can play an important role to promote the superconductivity, as found in the charge-ordered organic metals^{50,51}. This appears to be consistent with the enhanced superconducting gap ratio, found in IrTe₂ flakes (Fig. 4). Our results unveil the collaborating relationship, rather than the competing one, between the parent stripe and the superconducting orders in IrTe₂, highlighting IrTe₂ as a unique example among superconducting TMDCs. Further investigations, for examples, scanning tunnelling microscopy and spectroscopy as well as Raman spectroscopy below the T_c are highly desirable to identify the local superconducting gap structure along the charge modulation patterns and the electron-phonon coupling, which would elucidate the interplay of the stripe-charge-order and superconductivity in IrTe₂.

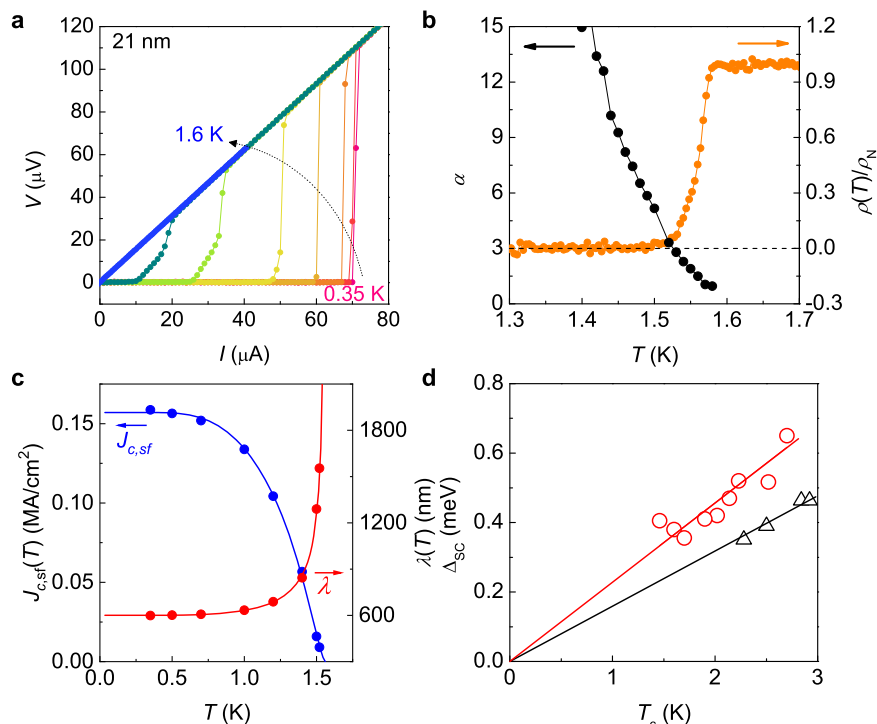


Fig. 4 Strong superconducting coupling in IrTe₂ nanoflakes. **a** Current-voltage (*IV*) characteristics at various temperatures for a representative IrTe₂ nanoflake with *d* = 21 nm. **b** Temperature dependence of the normalised resistivity and the exponent α for a 21-nm-thick IrTe₂ nanoflake. Exponent α is determined from the power-law behaviour $V \propto I^\alpha$ in the *IV* curves, as expected by BKT transition. **c** Critical current density (blue) and the penetration depth (red) as a function of temperature for a 21-nm-thick IrTe₂ nanoflake. Solid lines are the fits to the self-critical-current model described in the text. **d** Superconducting gap Δ_{sc} as a function of T_c , extracted from the critical current density for IrTe₂ nanoflakes with different *d* (red). The slope of their linear dependence, corresponding to the superconducting gap ratio, $2\Delta_{sc}/k_B T_c = 5.3$, is much larger than the case of doped bulk IrTe₂ (black) from refs. ^{37,42}. This difference confirms the strong coupling nature of the superconductivity in IrTe₂ nanoflakes.

Methods

Single crystal growth and bulk properties. IrTe₂ single crystals were synthesised using the Te-flux method³¹. Ir and Te powders were mixed in a stoichiometric ratio Ir:Te = 1:4, heated to 1160 °C for 1 day as sealed in a quartz ampoule, and then cooled. The crystallinity and stoichiometry were confirmed by X-ray diffraction and energy-dispersive X-ray spectroscopy.

Exfoliation and fabrication of nanoflakes. We used mechanical exfoliation of bulk single crystals to obtain thin nanoflakes of IrTe₂ on top of a Si/SiO₂ substrate that had been pre-cleaned in acetone, 2-propanol, and deionised water, then treated by oxygen plasma ($O_2 = 10$ sccm, $P \sim 100$ mTorr) for 5 min. All cleaving and handling were done in inert atmosphere ($H_2O < 0.1$ ppm, $O_2 < 0.1$ ppm) of pure Ar gas except the atomic force microscopy (AFM) measurements. In some cases, a thin h-BN crystal was subsequently transferred onto the IrTe₂ nanoflake in Ar atmosphere. We found that the optical contrast, the AFM thickness, and Raman spectra were unchanged even after 1 week in ambient conditions (Supplementary Fig. 1), indicating that the nanoflakes are stable in ambient conditions. To fabricate devices for electrical measurements, we used conventional e-beam lithography to pattern electrodes on top of IrTe₂ nanoflakes with metal deposition of Cr(10 nm)/Au(50 nm). The optical microscope image for the typical device is shown in Fig. 1f.

Transport property measurements. Transport measurements were performed in a cryogenic ³He refrigerator equipped with a superconducting vector magnet (9/2/2 T). Each measurement wire was filtered by a room-temperature π filter and low-temperature π and low-pass RC filters at 0.35 K to minimise the electrical noise on the sample. Electrical resistance was measured in standard four-probe configuration using DC delta mode with bias current 1 μ A to 10 μ A determined by the sample resistance and signal to noise ratio. Magnetic fields with desired field orientations were applied by the vector magnet at one cooling without altering sample position.

Raman spectroscopy. Raman spectra were obtained using a confocal microscopy set-up with laser beam size of ~ 1 μ m and laser power of ~ 1 mW. A

HeNe laser (632.8 nm) was used to excite IrTe₂ flakes in an optical cryostat at normal incidence. The Raman signal was collected in the backscattering configuration and analysed using a monochromator equipped with a liquid nitrogen-cooled silicon CCD. Two linear polarizers in the parallel configuration were placed immediately after the laser and before the monochromator to define the polarization of incident and scattered light, respectively. The crystal orientation relative to the polarisation of the incident light was controlled using a half waveplate between a beam splitter and IrTe₂ flakes. The sample position was precisely controlled using a piezo stage.

Scanning tunnelling microscopy and spectroscopy. For scanning tunnelling microscopy (STM) and spectroscopy (STS) measurements, IrTe₂ nanoflakes were exfoliated in a glove box ($H_2O < 0.1$ ppm, $O_2 < 0.1$ ppm) filled with Ar gas, and transferred onto graphene, grown epitaxially on a 4H-SiC(0001) substrate. The samples were then transferred to an ultrahigh vacuum chamber ($P \leq 1 \times 10^{-10}$ Torr) for STM/STS measurements without any exposure to air to ensure clean surfaces of IrTe₂ nanoflakes. STM images were typically obtained using a bias voltage $V_b = -2.5$ V and a tunnelling current $I_t = 20$ pA for large-scale imaging; $V_b = 15$ mV and $I_t = 1$ nA for charge-ordered stripe phases; $V_b = 5$ mV and $I_t = 2$ nA for atomically-resolved images. For STS, we used the lock-in technique with a bias modulation of 7 mV_{rms}.

Density functional theory calculations. Density functional theory (DFT) calculations for electronic structures and the electron-phonon coupling (EPC) were performed by the Quantum Espresso package implementing the pseudo-potential band method and the density functional perturbation theory^{52,53}. We utilised Perdew-Burke-Ernzerhof sol (PBEsol, revised PBE for solid)⁵⁴ as an exchange-correlation functional and included the spin-orbit coupling (SOC). The dynamical matrices were calculated using $2 \times 2 \times 2$ *q*-mesh and $16 \times 10 \times 4$ *k*-mesh with 40 Ry energy cutoff. We applied the various in-plane tensile strains in the range of $\Delta a/a \sim 2.1$ –3.1% and the fixed compressive strain of $\Delta b/b \sim 0.65\%$ to model the experimental situations (Supplementary Note 6). Atomic positions were optimised in each case.

Data availability

The data that support the findings of this study are available from the corresponding authors on request.

Received: 25 October 2020; Accepted: 21 April 2021;

Published online: 26 May 2021

References

- Wilson, J. A., Salvo, F. J. D. & Mahajan, S. Charge-density waves and superlattices in the metallic layered transition metal dichalcogenides. *Adv. Phys.* **24**, 117–201 (1975).
- Sipos, B. et al. From Mott state to superconductivity in 1T-TaS₂. *Nat. Mater.* **7**, 960–965 (2008).
- Joe, Y. I. et al. Emergence of charge density wave domain walls above the superconducting dome in 1T-TiSe₂. *Nat. Phys.* **10**, 421–425 (2014).
- Kogar, A. et al. Observation of a charge density wave incommensuration near the superconducting dome in Cu_xTiSe₂. *Phys. Rev. Lett.* **118**, 27002 (2017).
- Yan, S. et al. Influence of domain walls in the incommensurate charge density wave state of Cu intercalated 1T-TiSe₂. *Phys. Rev. Lett.* **118**, 106405 (2017).
- Cercellier, H. et al. Evidence for an excitonic insulator phase in 1T-TiSe₂. *Phys. Rev. Lett.* **99**, 146403 (2007).
- Wagner, K. E. et al. Tuning the charge density wave and superconductivity in Cu_xTaS₂. *Phys. Rev. B* **78**, 104520 (2008).
- Morosan, E. et al. Superconductivity in Cu_xTiSe₂. *Nat. Phys.* **2**, 544–550 (2006).
- Si, Q. & Steglich, F. Heavy fermions and quantum phase transitions. *Science* **329**, 1161–1166 (2010).
- Lee, P. A., Nagaosa, N. & Wen, X.-G. Doping a Mott insulator: Physics of high-temperature superconductivity. *Rev. Mod. Phys.* **78**, 17 (2006).
- Stewart, G. Superconductivity in iron compounds. *Rev. Mod. Phys.* **83**, 1589 (2011).
- Novoselov, K. S. et al. Two-dimensional atomic crystals. *Proc. Natl Acad. Sci. USA* **102**, 10451–10453 (2005).
- Yoshida, M. et al. Controlling charge-density-wave states in nano-thick crystals of 1T-TaS₂. *Sci. Rep.* **4**, 7302 (2014).
- Yu, Y. et al. Gate-tunable phase transitions in thin flakes of 1T-TaS₂. *Nat. Nanotechnol.* **10**, 270–276 (2015).
- Navarro-Moratalla, E. et al. Enhanced superconductivity in atomically thin TaS₂. *Nat. Commun.* **7**, 1–7 (2016).
- Xi, X. et al. Strongly enhanced charge-density-wave order in monolayer NbSe₂. *Nat. Nanotechnol.* **10**, 765–769 (2015).
- Xi, X. et al. Ising pairing in superconducting NbSe₂ atomic layers. *Nat. Phys.* **12**, 139–143 (2016).
- Pyon, S., Kudo, K. & Nohara, M. Superconductivity induced by bond breaking in the triangular lattice of IrTe₂. *J. Phys. Soc. Jpn.* **81**, 53701 (2012).
- Yang, J. J. et al. Charge-orbital density wave and superconductivity in the strong spin-orbit coupled IrTe₂/Pd. *Phys. Rev. Lett.* **108**, 116402 (2012).
- Kudo, K., Kobayashi, M., Pyon, S. & Nohara, M. Suppression of structural phase transition in IrTe₂ by isovalent Rh doping. *J. Phys. Soc. Jpn.* **82**, 85001 (2013).
- Kamitani, M. et al. Superconductivity in Cu_xIrTe₂ driven by interlayer hybridization. *Phys. Rev. B* **87**, 180501 (2013).
- Fujisawa, Y. et al. Visualizing the Pt doping effect on surface and electronic structure in Ir_{1-x}Pt_xTe₂ by scanning tunneling microscopy and spectroscopy. *J. Phys. Soc. Jpn.* **84**, 43706 (2015).
- Takubo, K. et al. Commensurate versus incommensurate charge ordering near the superconducting dome in Ir_{1-x}Pt_xTe₂ revealed by resonant x-ray scattering. *Phys. Rev. B* **97**, 205142 (2018).
- Oh, Y. S., Yang, J. J., Horibe, Y. & Cheong, S.-W. Anionic depolymerization transition in IrTe₂. *Phys. Rev. Lett.* **110**, 127209 (2013).
- Ko, K.-T. et al. Charge-ordering cascade with spin-orbit Mott dimer states in metallic iridium ditelluride. *Nat. Commun.* **6**, 7342 (2015).
- Hsu, P.-J. et al. Hysteretic melting transition of a soliton lattice in a commensurate charge modulation. *Phys. Rev. Lett.* **111**, 266401 (2013).
- Daiki, O. et al. Electronic structure reconstruction by orbital symmetry breaking in IrTe₂. *J. Phys. Soc. Jpn.* **82**, 93704 (2013).
- Kim, K. et al. Origin of first-order-type electronic and structural transitions in IrTe₂. *Phys. Rev. Lett.* **114**, 136401 (2015).
- Rahn, D. J. et al. Gaps and kinks in the electronic structure of the superconductor 2H-NbSe₂ from angle-resolved photoemission at 1 K. *Phys. Rev. B* **85**, 224532 (2012).
- Pascut, G. L. et al. Dimerization-induced cross-layer quasi-two-dimensionality in metallic IrTe₂. *Phys. Rev. Lett.* **112**, 86402 (2014).
- Eom, M. J. et al. Dimerization-induced fermi-surface reconstruction in IrTe₂. *Phys. Rev. Lett.* **113**, 266406 (2014).
- Yoshida, M., Kudo, K., Nohara, M. & Iwasa, Y. Metastable superconductivity in two-dimensional IrTe₂ crystals. *Nano Lett.* **18**, 3113–3117 (2018).
- Oike, H., Kamitani, M., Tokura, Y. & Kagawa, F. Kinetic approach to superconductivity hidden behind a competing order. *Sci. Adv.* **4**, eaau3489 (2018).
- Oike, H. et al. Size effects on supercooling phenomena in strongly correlated electron systems: IrTe₂ and θ -(BEDT-TTF)₂RbZn(SCN)₄. *Phys. Rev. B* **97**, 85102 (2018).
- Kim, H. S. et al. Nanoscale superconducting honeycomb charge order in IrTe₂. *Nano Lett.* **16**, 4260–4265 (2016).
- Glamazda, A., Choi, K.-Y., Lemmens, P., Yang, J. J. & Cheong, S.-W. Proximity to a commensurate charge modulation in IrTe_{2-x}Se_x ($x = 0$ and 0.45) revealed by Raman spectroscopy. *N. J. Phys.* **16**, 93061 (2014).
- Yu, D. J. et al. Fully gapped s -wave-like superconducting state and electronic structure in Ir_{0.95}Pd_{0.05}Te₂ single crystals with strong spin-orbital coupling. *Phys. Rev. B* **89**, 100501 (2014).
- Tinkham, M. *Introduction to Superconductivity*. (Dover Publications, Inc., New York, 2004).
- Zhou, S. Y. et al. Nodeless superconductivity in Ir_{1-x}Pt_xTe₂ with strong spin-orbital coupling. *Europhys. Lett.* **104**, 27010 (2013).
- Talantsev, E. F. & Tallon, J. L. Universal self-field critical current for thin-film superconductors. *Nat. Commun.* **6**, 7820 (2015).
- Talantsev, E. F. et al. On the origin of critical temperature enhancement in atomically thin superconductors. *2D Mater.* **4**, 25072 (2017).
- Wilson, M. N. et al. μ SR and magnetometry study of superconducting 5% Pt-doped IrTe₂. *Phys. Rev. B* **94**, 184504 (2016).
- Pascut, G. L. et al. Series of alternating states with unpolarized and spin-polarized bands in dimerized IrTe₂. *Phys. Rev. B* **90**, 195122 (2014).
- Rumo, M. et al. Examining the surface phase diagram of IrTe₂ with photoemission. *Phys. Rev. B* **101**, 235120 (2020).
- Li, Q. et al. Bond competition and phase evolution on the IrTe₂ surface. *Nat. Commun.* **5**, 5358 (2014).
- Yoshida, M. et al. Extended polymorphism of two-dimensional material. *Nano Lett.* **17**, 5567–5571 (2017).
- Nicholson, C. W. et al. Uniaxial strain-induced phase transition in the 2D topological semimetal IrTe₂. *Commun. Mater.* **2**, 1–8 (2021).
- Merino, J. & McKenzie, R. H. Superconductivity mediated by charge fluctuations in layered molecular crystals. *Phys. Rev. Lett.* **87**, 237002 (2001).
- Foussats, A., Greco, A., Bejas, M. & Muramatsu, A. Cooperative effect of phonons and electronic correlations for superconductivity in cobaltates. *Phys. Rev. B* **72**, 020504 (2005).
- Kaiser, S. et al. Bandwidth tuning triggers interplay of charge order and superconductivity in two-dimensional organic materials. *Phys. Rev. Lett.* **105**, 206402 (2010).
- Girlando, A. et al. Charge-order fluctuations and superconductivity in two-dimensional organic metals. *Phys. Rev. B* **89**, 174503 (2014).
- Giannozzi, P. et al. QUANTUM ESPRESSO: a modular and open-source software project for quantum simulations of materials. *J. Phys.: Condens. Matter* **21**, 395502 (2009).
- Baroni, S., De Gironcoli, S., Dal Corso, A. & Giannozzi, P. Phonons and related crystal properties from density-functional perturbation theory. *Rev. Mod. Phys.* **73**, 515 (2001).
- Perdew, J. P. et al. Restoring the density-gradient expansion for exchange in solids and surfaces. *Phys. Rev. Lett.* **100**, 136406 (2008).

Acknowledgements

The authors thank K.T. Ko, G.Y. Jo, Y.K. Bang for fruitful discussion. We also thank H. G. Kim in Pohang Accelerator Laboratory (PAL) for the technical support. This work was supported by the Institute for Basic Science (IBS) through the Center for Artificial Low Dimensional Electronic Systems (no. IBS-R014-D1), the National Research Foundation of Korea (NRF) through SRC (Grant No. NRF-2018R1A5A6075964), and the Max Planck-POSTECH Center for Complex Phase Materials (Grant No. NRF-2016K1A4A4A01922028). J.K., M.J.K. acknowledge the support from the NRF of Korea grant (Grant No. NRF-2017R1C1B2012729 and NRF-2020R1A4A1018935). K.W. and T.T. acknowledge support from the Elemental Strategy Initiative conducted by the MEXT, Japan, Grant Number JPMXP0112101001, JSPS KAKENHI Grant Numbers JP20H00354 and the CREST (JPMJCR15F3), JST. E. F. T. thanks financial support provided by the state assignment of Minobnauki of Russia (theme Pressure No. AAAA-A18-118020190104-3) and by Act 211 Government of the Russian Federation, contract no. 02.A03.21.0006. S.K. acknowledges the support from the NRF of Korea grant (Grant No. NRF-2019R1F1A1052026) and KISTI supercomputing center (Grant No. KSC-2019-CRE-0172). K.K. acknowledges the support from the NRF of Korea grant (Grant No. 2016R1D1A1B02008461) and Internal R&D programme at KAERI (Grant No. 5244460-21). SWC was partially supported by the NSF under Grant No. DMR-1629059.

Author contributions

S.P., S.Y.K., and J.S.K. conceived the experiments. S.Y.K. and S.P. fabricated the devices. S.P., S.Y.K., G.S.C., and E.F.T. performed transport property measurements and data analysis. H.K.K., H.W.Y., and T.-H.K. performed scanning tunnelling microscopy/spectroscopy and data analysis. M.J.K., S.Y.K., T. K., H.K., B.J.K., and J.K. performed Raman spectroscopy and data analysis. S.K. and K.K. performed density functional theory calculation and analysis. C.J.W. and S.-W.C. synthesised the bulk crystals. K.W. and T.T. provided boron nitride crystals. S.P., S.Y.K., J.K., T.-H.K., and J.S.K. co-wrote the manuscript. All authors discussed the results and commented on the paper.

Competing interests

The authors declare no competing interests.

Additional information

Supplementary information The online version contains supplementary material available at <https://doi.org/10.1038/s41467-021-23310-w>.

Correspondence and requests for materials should be addressed to J.K., T.-H.K. or J.S.K.

Peer review information *Nature Communications* thanks the anonymous reviewer(s) for their contribution to the peer review of this work. Peer reviewer reports are available.

Reprints and permission information is available at <http://www.nature.com/reprints>

Publisher's note Springer Nature remains neutral with regard to jurisdictional claims in published maps and institutional affiliations.



Open Access This article is licensed under a Creative Commons Attribution 4.0 International License, which permits use, sharing, adaptation, distribution and reproduction in any medium or format, as long as you give appropriate credit to the original author(s) and the source, provide a link to the Creative Commons license, and indicate if changes were made. The images or other third party material in this article are included in the article's Creative Commons license, unless indicated otherwise in a credit line to the material. If material is not included in the article's Creative Commons license and your intended use is not permitted by statutory regulation or exceeds the permitted use, you will need to obtain permission directly from the copyright holder. To view a copy of this license, visit <http://creativecommons.org/licenses/by/4.0/>.

© The Author(s) 2021